

Large-Eddy Simulations of Atmospheric Flows Over Complex Terrain Using the Immersed-Boundary Method in the Weather Research and Forecasting Model

Yulong Ma¹ · Heping Liu¹

Received: 8 October 2016 / Accepted: 4 July 2017 / Published online: 21 July 2017
© Springer Science+Business Media B.V. 2017

Abstract Atmospheric flow over complex terrain, particularly recirculation flows, greatly influences wind-turbine siting, forest-fire behaviour, and trace-gas and pollutant dispersion. However, there is a large uncertainty in the simulation of flow over complex topography, which is attributable to the type of turbulence model, the subgrid-scale (SGS) turbulence parametrization, terrain-following coordinates, and numerical errors in finite-difference methods. Here, we upgrade the large-eddy simulation module within the Weather Research and Forecasting model by incorporating the immersed-boundary method into the module to improve simulations of the flow and recirculation over complex terrain. Simulations over the Bolund Hill indicate improved mean absolute speed-up errors with respect to previous studies, as well as an improved simulation of the recirculation zone behind the escarpment of the hill. With regard to the SGS parametrization, the Lagrangian-averaged scale-dependent Smagorinsky model performs better than the classic Smagorinsky model in reproducing both velocity and turbulent kinetic energy. A finer grid resolution also improves the strength of the recirculation in flow simulations, with a higher horizontal grid resolution improving simulations just behind the escarpment, and a higher vertical grid resolution improving results on the lee side of the hill. Our modelling approach has broad applications for the simulation of atmospheric flows over complex topography.

Keywords Bolund Hill experiment · Complex terrain · Immersed-boundary method · Large-eddy simulation · Weather Research and Forecasting model

1 Introduction

There is a growing demand for accurate and efficient numerical modelling of atmospheric boundary-layer (ABL) flows over complex terrain. However, the prediction of complex tur-

✉ Heping Liu
heping.Liu@wsu.edu

¹ Department of Civil and Environmental Engineering, Washington State University, Pullman, WA 99164, USA

bulent flow is still problematic, particularly in places where recirculation occurs (Lopes et al. 2007; Diebold et al. 2013; Abdi and Bitsuamlak 2014), which affects atmospheric-flow patterns, and influences the mass and energy transport in the ABL over complex terrain. Thus, the accurate simulation of recirculation is important for many diverse applications, including wind-turbine siting (Yang et al. 2015a), the prediction of forest-fire behaviour (Simpson et al. 2013), and the distribution of air pollution in urban environments (Lateb et al. 2016).

Previous numerical studies indicate that, even over gently sloped topography, the accurate simulation of recirculation on the lee side of hills continues to be a challenge (Castro et al. 2003; Lopes et al. 2007; Bechmann and Sørensen 2010), with several factors being particularly influential. For example, a reliable wall-function model of the surface momentum flux improves simulations (Kim and Patel 2000), because surface friction and fluxes contribute greatly to the intensity of wake vorticity on the lee side of a hill (Ding and Street 2003), while higher grid resolutions lead to improved results (Castro et al. 2003). Apart from these two factors, it is believed that the turbulence-modelling methods currently employed also have a crucial impact on the accurate simulation of recirculation flow.

Common turbulence-modelling methods include approximations to the Reynolds-averaged Navier–Stokes (RANS) equations and large-eddy simulation (LES), where a time-averaged flow is simulated with consideration of the entire spectrum of turbulence in the former, while only a certain range of large-scale turbulence is explicitly resolved with the latter. Previous research has shown that the well-known two-equation turbulence models, such as the so-called $k - \epsilon$ and $k - \omega$ RANS turbulence models, often generate a suppressed recirculation flow (Bechmann and Sørensen 2010; Prospathopoulos et al. 2012; Abdi and Bitsuamlak 2014), with LES models generally able to generate a more realistic recirculation than these turbulence models (Lopes et al. 2007; Bechmann and Sørensen 2010).

However, the performance of a LES model is largely dependent on the choice of the subgrid-scale (SGS) model. For example, the two commonly used SGS models for the simulation of the ABL are the Smagorinsky model (Smagorinsky 1963) and the 1.5-order turbulent kinetic energy (TKE) model (Deardorff 1980), which are believed to suppress the intensity of recirculation (Allen and Brown 2002; Chow and Street 2009) due to the constant eddy viscosity coefficient, which results in excess turbulence dissipation of the resolved turbulence (Mirocha et al. 2010; Kirkil et al. 2012). Alternatively, dynamic-coefficient models calculate the eddy viscosity based on certain characteristics of the turbulent flow. For example, the Lagrangian-averaged scale-dependent Smagorinsky model (hereafter the LASD model; Porté-Agel et al. 2000; Bou-Zeid et al. 2005) significantly improves the simulation of recirculation over complex terrain compared with a constant-coefficient approach, in conjunction with the use of pseudo-spectral methods (Tseng et al. 2006; Wan and Porté-Agel 2011; Diebold et al. 2013). In the framework of finite-difference methods, simulations over flat or simple topography indicate that the LASD model behaves differently than when used with pseudo-spectral methods, resulting in more dissipative behaviour (Kirkil et al. 2012; Mirocha et al. 2013; Xie et al. 2015). Moreover, the odd-ordered, upwind-biased finite-difference advection schemes induce extra numerical diffusion (Knievel et al. 2007; Kirkil et al. 2012; Xie et al. 2015), which may also influence the accurate simulation of recirculation with the LASD model, since more energy is dissipated into subgrid scales. Hence, although widely used for pseudo-spectral methods, the LASD model has received less attention for the simulation of the ABL (Kirkil et al. 2012; Mirocha et al. 2014; Xie and Archer 2015).

Over highly complex terrain marked by steep slopes, it is even more challenging to perform a reliable simulation of turbulence. Atmospheric numerical models often use terrain-following coordinates that induce significant errors, and result in numerical instability over steep slopes (Klemp et al. 2003). Alternatively, while computational fluid dynamics (CFD) models (e.g., OpenFOAM and Fluent) using body-fitted coordinates have been used to simulate ABL flows (Prospathopoulos et al. 2012; Abdi and Bitsuamlak 2014; Vuorinen et al. 2015; Cavar et al. 2016), drawbacks include the lack of options for representing atmospheric processes, and the time-consuming generation of body-fitted grids. Recently, the immersed-boundary method, first proposed by Peskin (1972), has been used together with LES modelling (Tseng et al. 2006; Bou-Zeid et al. 2009; Lundquist et al. 2012; Diebold et al. 2013) for representing complex terrain in Cartesian coordinates. The coordinate-transformation errors in terrain-following coordinate models are thereby eliminated, and problems of numerical instability in traditional atmospheric numerical models over steep terrain are mitigated. Moreover, such models benefit from both the rich physical packages existing within numerical models, as well as the more rapid generation of grids over highly complex topography.

Lundquist et al. (2010, 2012) have incorporated a relatively simple immersed-boundary method into the LES module of the Weather Research and Forecasting (WRF) model (Skamarock et al. 2008), which is a widely-used numerical model with finite-difference discretization methods and terrain-following coordinates, and has been extensively validated for different applications (e.g., Moeng et al. 2007; Mirocha et al. 2010, 2013, 2014; Kirkil et al. 2012; Talbot et al. 2012; Zhang et al. 2013; Udina et al. 2016). The immersed-boundary method within the WRF model uses a linear velocity profile near the surface (hereafter the linear method), which is strictly valid for low- and moderate-Reynolds-number flows, or for idealized ABL flows with a grid resolution that resolves the viscous sublayer explicitly (Mittal and Iaccarino 2005). Another immersed-boundary method (Chester et al. 2007) adopts a wall-function model near the immersed surface, reconstructs a constant layer of near-surface turbulence stress (hereafter the stress method), and simulates turbulent flows over complex terrain realistically (Diebold et al. 2013). However, the near-surface stresses, which are based on the assumption of a logarithmic velocity profile, are problematic for separated flows over complex terrain, for which a more sophisticated wall model is required (i.e., Yang et al. 2015b; Sadique et al. 2017).

Therefore, we incorporate a number of state-of-the-art modules into the WRF model for the study of atmospheric flows, with a particular emphasis on recirculation, by including the LASD model (Bou-Zeid et al. 2005) (which was first implemented into the WRF model by Kirkil et al. 2012, but the code was not released) and the stress method (Chester et al. 2007), to make it the first such modelling system within the LES module of the WRF model. To provide more realistic horizontal boundary conditions over complex terrain, we implement a turbulent inflow at the inlet as opposed to the default periodic boundary conditions. Our approach is tested over the Bolund Hill under neutral stability conditions; due to the sharp vertical escarpment of the Bolund Hill, the recirculation has not been reproduced well in previous simulations. For example, most numerical models overpredict the speed-up behind the escarpment (Prospathopoulos et al. 2012; Vuorinen et al. 2015; Cavar et al. 2016).

Below, the numerical methods and simulation set-up are described in Sects. 2 and 3, simulation results are analyzed and compared with observations in Sect. 4, the numerical diffusion is examined in Sect. 5, and our conclusions are provided in Sect. 6.

2 Numerical Methods

2.1 Large-Eddy Simulation

The WRF model is a widely-used atmospheric modelling system for flow simulation at scales from the mesoscale to the local scale. The latest WRF model is version 3.9 released on April 17 2017. The LES module within the WRF model, which has been used by [Moeng et al. \(2007\)](#), [Mirocha et al. \(2010, 2013\)](#), [Kirkil et al. \(2012\)](#), applies a low-pass filter to separate large from small eddies, where the large eddies are explicitly resolved, and the small eddies are parametrized by the SGS model. Since the grid spacing acts as an implicit low-pass filter, the unresolved stresses τ_{ij} must be modelled based on the resolved velocity. With the eddy-viscosity hypothesis, the unresolved stresses can be expressed as

$$\tau_{ij} - \frac{1}{3}\delta_{ij}\tau_{kk} = -2\nu_t\tilde{S}_{ij}. \tag{1}$$

Here, δ_{ij} is the Kronecker delta, ν_t is the eddy viscosity, and \tilde{S}_{ij} is the resolved strain-rate tensor defined as

$$\tilde{S}_{ij} = \frac{1}{2}\left(\frac{\partial\tilde{u}_i}{\partial x_j} + \frac{\partial\tilde{u}_j}{\partial x_i}\right), \tag{2}$$

where \tilde{u}_i (\tilde{u}_j) ($i, j = 1, 2, 3$) are the resolved/filtered velocity components in the (x, y, z) directions.

The determination of ν_t is a critical aspect, which the Smagorinsky model expresses as

$$\nu_t = (C_{s,\Delta}\Delta)^2|\tilde{S}|, \tag{3}$$

where $C_{s,\Delta}$ is the Smagorinsky coefficient (a constant), Δ is the grid spacing, and $|\tilde{S}|$ is the magnitude of the resolved strain-rate tensor. As we find the default value of $C_{s,\Delta} = 0.25$ to be too large for simulations over the Bolund Hill, we apply the smaller value of 0.15. The WRF model also includes the 1.5-order TKE parametrization, which gives a nearly identical performance to the Smagorinsky model in idealized, neutrally-buoyant simulations ([Kirkil et al. 2012](#)). Thus, only the Smagorinsky model is considered here.

As constant-coefficient models perform poorly in simulating recirculation flows due to excess dissipation near the surface ([Wan and Porté-Agel 2011](#); [Kirkil et al. 2012](#)), an alternative is to compute $C_{s,\Delta}$ dynamically based on the resolved velocities. One such dynamic-coefficient approach is the LASD model ([Bou-Zeid et al. 2005](#)), which utilizes two explicit filters of twice and quadruple the sizes of the grid spacing for evaluating the scale-dependent coefficients, $C_{s,2\Delta}$ and $C_{s,4\Delta}$, respectively. [Bou-Zeid et al. \(2005\)](#) assumed a power-law dependence of these coefficients, which yields

$$C_{s,\Delta}^2 = C_{s,2\Delta}^2 / (C_{s,4\Delta}^2 / C_{s,2\Delta}^2). \tag{4}$$

Here, the Smagorinsky coefficient $C_{s,\alpha\Delta}$ at two explicit filter scales ($\alpha = 2, 4$) is calculated as

$$C_{s,\alpha\Delta}^2 = \frac{\langle L_{ij,\alpha\Delta} M_{ij,\alpha\Delta} \rangle}{\langle M_{ij,\alpha\Delta} M_{ij,\alpha\Delta} \rangle}, \tag{5}$$

where the angled brackets ($\langle \rangle$) represent the Lagrangian averaging along the fluid trajectory, which limits numerical instabilities. Here, $L_{ij,\alpha\Delta}$ and $M_{ij,\alpha\Delta}$ are given by

$$L_{ij,\alpha\Delta} = \widetilde{\widetilde{u}_i u_j} - \widetilde{u}_i \widetilde{u}_j \tag{6}$$

and

$$M_{ij,\alpha\Delta} = 2\Delta^2 \left(\overline{\left| \widetilde{S} \right| \overline{S_{i,j}}} - \alpha^2 \overline{\left| \widetilde{S} \right| \overline{S_{i,j}}} \right), \quad (7)$$

where the overbar denotes test-filtering at a scale of $\alpha\Delta$. Note that the scale-dependent parameter β , which was expressed in terms of $M_{ij,\alpha\Delta}$ in Bou-Zeid et al. (2005), is set to unity here.

The LASD model has been incorporated into the WRF model, and validated over simple topography, including flat terrain and a two-dimensional hill, by Kirkil et al. (2012). The two explicit filters may be either top-hat or Gaussian filters, and since the performance of the top-hat filter is superior to the Gaussian filter (Xie et al. 2015), we use the top-hat filter. For example, a one-dimensional top-hat filter for the field variable ϕ at location x_0 is written as

$$\overline{\phi(x_0)} = \int_{x_0 - \frac{\Delta}{2}}^{x_0 + \frac{\Delta}{2}} \frac{1}{\Delta} \phi(x) dx, \quad (8)$$

which is repeated in the x , y , and z directions in the case of a three-dimensional top-hat filter.

Aliasing and discretization schemes result in numerical errors (Chow and Moin 2003). In the WRF model, the divergence form of the non-linear convective term (aliasing), together with the fifth- and third-order differencing method in the horizontal and vertical directions, respectively, may generate non-negligible errors (Kirkil et al. 2012; Talbot et al. 2012; Xie et al. 2015). The odd-ordered, upwind-biased advection schemes in the WRF model are numerically diffusive (Knievel et al. 2007) in the sense that resolved energy is dissipated at the subgrid scale. We examine the significance of numerical diffusion below.

For simulations over complex topography with large-eddy simulation, it is more appropriate to apply realistic inflow boundary conditions than the periodic horizontal boundary conditions, although, for this particular case, the periodic boundary conditions are acceptable since the Bolund Hill is relatively low. To provide a realistic turbulent inflow, we perform a precursor simulation identical to Chow and Street (2009) over a flat terrain with periodic boundary conditions, with the same grid configuration as the simulations over complex terrain. A constant pressure gradient driving the flow is applied along the streamwise direction in the precursor simulation, whose magnitude is specified to ensure the mean velocity profile is close to that desired. The velocity data are extracted from a slice and stored every timestep once the flow reaches a statistically stationary state. The turbulent inflow is enforced at the western lateral boundary, a zero-gradient boundary is set at the eastern boundary, and the periodic boundary conditions are set at both the northern and southern boundaries. The outflow at the eastern boundary is set as zero-gradient for simplicity, where Lund et al. (1998) and Lopes et al. (2007) used a convective boundary.

2.2 Immersed-Boundary Method

The immersed-boundary method is a numerical method for handling complex geometry in Cartesian coordinates, by enforcing the boundary conditions at the grid nodes near the surface. A number of variants for treating the effect of the immersed surface exists, including the direct-forcing method first proposed by Mohd-Yusof (1997), which modifies the velocity or stress near the grid nodes at the surface, with no further additional terms considered. Both the linear method and the stress method are categorized as the direct forcing method. To save computational time, subroutines are called each of the three Runge–Kutta (large) timesteps, but not each acoustic timestep.

The linear method implemented into the WRF model by Lundquist et al. (2010, 2012) uses the “ghost-cell” method to represent the immersed surface in Cartesian coordinates,

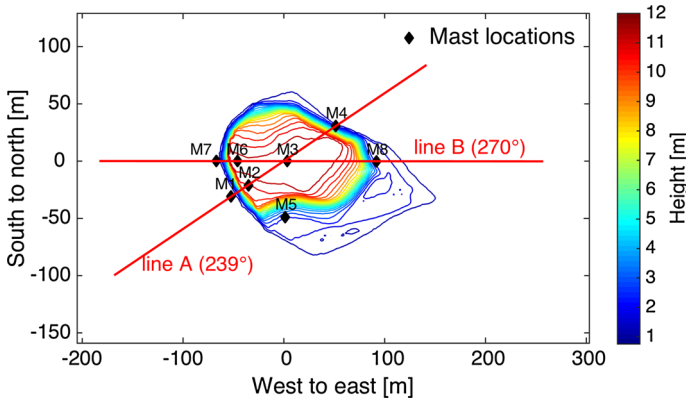


Fig. 1 Topographic map and the measurement locations (M1–M8) of the Bolund Hill experiment

where a ghost cell is defined as the first grid node below the surface. If a no-slip boundary condition (i.e., a zero velocity at the surface boundary) is applied, the ghost-cell velocity components are reconstructed using

$$\phi_G = -\phi_I, \tag{9}$$

where ϕ_G is the velocity component at a ghost point, and ϕ_I is the velocity at the image point defined as the ghost point mirrored over the surface. Hence, Eq. 9 shows that the velocity components are assumed to vary linearly near the surface, where ϕ_I is interpolated from the surrounding points above the immersed surface, for which we apply the inverse-distance-weighted interpolation suggested by Lundquist et al. (2012). The key step is, however, to identify the image point (or the wall-normal direction) in a three-dimensional topography, for which we adopt the method proposed by Mittal et al. (2008) for identification of the wall-normal direction.

As the linear method is invalid in simulations of the ABL flows in which the viscous sublayer is not explicitly resolved (Senocak et al. 2004), we incorporate the stress method of Chester et al. (2007) into the WRF model. The stress method modifies the subgrid stresses instead of the velocities at the grid nodes near the immersed surface, with the assumption of the existence of a constant layer of subgrid stress, τ_s , above the immersed surface in the surface-normal direction. The thickness of the layer is slightly greater than the grid spacing, and τ_s , which is defined as parallel to the local surface, is calculated from the logarithmic velocity profile. All SGS components at grid nodes within the constant-stress layer are reconstructed from τ_s . In addition, a second layer below the surface is used as a smooth transition, where the subgrid stresses are extrapolated from the above layers. The velocities at the grid nodes below the immersed surface are all set to zero at the end of each timestep. Since it is no longer necessary to use the finite-difference method, the stress method of Chester et al. (2007) is modified to neglect the smoothing of the horizontal-plane stress further inside the immersed surface (e.g., below the second layer). A detailed description of the implementation of the stress method is provided in Appendix 1.

3 Simulation Set-Up

3.1 The Bolund Hill Experiment

The upgraded modelling system is used to simulate the flow over the Bolund Hill for examination of its performance in reproducing recirculation flows; a detailed description of the experiment at Bolund Hill is provided in [Berg et al. \(2011\)](#) and [Bechmann et al. \(2011\)](#). Briefly, the experiment was conducted from December 2008 to February 2009 on the Bolund Hill, which is located north of Risø Technical University of Denmark. The Bolund Hill is 12-m high, 130-m long, and 75-m wide, and is surrounded by sea on all sides, except for the eastern side (Fig. 1). Although the hill is relatively small, the steep slope and the 10-m escarpment on the western side of the hill induce complex flow patterns. During the campaign, velocities from four different directions (270° , 255° , 239° and 90°) were measured at ten observational sites (M0–M9) using 35 anemometers. The M0 and M9 sites further to the west and east, respectively, act as the reference sites for the inflow conditions, while the sites M1–M8 around the hill provide the comparison data. The measured velocity data are averaged in time for 10-min intervals, while the atmosphere is considered to be neutral during the observational periods.

3.2 Model Configurations

We use a computational domain size of $510 \text{ m} \times 290 \text{ m} \times 120 \text{ m}$ in the x , y , and z directions (Fig. 1), respectively, with a uniform roughness length (0.3 and 15 mm for flow originating from water and land, respectively), which is similar to that used by [Diebold et al. \(2013\)](#). We designed two sets of grid resolutions to investigate the impact on simulations. For the coarse-resolution runs, the horizontal grid spacing is $dx = dy = 2 \text{ m}$. In the vertical direction, a constant grid resolution $dz = 0.5 \text{ m}$ is set below 25 m and stretched above, resulting in a maximum grid spacing of approximately 3 m at the domain top. The vertical resolution yields an aspect ratio $dx/dz = 4$ near the surface, as recommended by [Mirocha et al. \(2010\)](#) and [Kirkil et al. \(2012\)](#). In the fine-resolution runs, the grid spacing is half the resolution of the coarse runs, with a horizontal grid spacing of 1 m and a vertical grid spacing of 0.25 below 25 m. At the top of the domain, the vertical velocity component w is set to zero, with u and v following free-slip conditions. Also, a 12-m Rayleigh damping layer is applied to w at the domain top (i.e., 10% of the domain height). Fifth- and third-order upwind-biased spatial-differencing methods are deployed for the horizontal and vertical advection, respectively. The non-linear convective term is the default divergence form. The lateral boundary conditions to the south and north are periodic, the turbulent inflow is applied to the western boundary, and the zero-gradient condition to the eastern boundary. Since the height of the hill is much lower than the height of the ABL, Coriolis effects are neglected ([Berg et al. 2011](#)). A constant pressure-gradient forcing ($8 \times 10^{-4} \text{ m s}^{-2}$) in the streamwise (x) direction drives the flow in the precursor simulation for generation of the turbulent inflow, and is also used in the 'real' runs in the streamwise direction for maintaining the velocity through the domain. Each simulation runs for 12 min, with the first 2 min considered as spin-up time (approximately nine advection times along the hill). Output data are averaged over the last 10 min, and are saved at 5-s intervals during the averaging period.

Simulations are performed for four different wind directions (270° , 255° , 239° and 90°), with the topography rotated to ensure inflow from the west of the domain, where the turbulent inflow is applied with wind-speed profiles following [Bechmann et al. \(2011\)](#). The first three cases (270° , 255° and 239° with flow from the sea) use the same wind-speed profile of the

Table 1 List of the simulation cases, with all three runs using the stress method

Run name	SGS model	Resolution
LASD-dx2m	LASD	$dx = dy = 2 \text{ m}, dz = 0.5 \text{ m}$
LASD-dx1m	LASD	$dx = dy = 1 \text{ m}, dz = 0.25 \text{ m}$
Smag-dx2m	Smagorinsky	$dx = dy = 2 \text{ m}, dz = 0.5 \text{ m}$

inflow, with a friction velocity of 0.4 m s^{-1} and a roughness length of 0.3 mm . The fourth case (90° with flow from the land) uses a logarithmic velocity profile, with a friction velocity of 0.5 m s^{-1} , and a roughness length of 15 mm . The mean velocity profiles at the inflow boundary agree well with the suggested logarithmic profile (not shown).

Both the linear and stress methods have been tested using the coarse resolution over the Bolund Hill, with the linear method performing worse than the stress method (see Sect. 4.1). Therefore, we limit discussion to simulations of the stress method for all four wind directions, and with different grid resolutions and SGS models (see Table 1). Note that there is no Smagorinsky run at a 1-m grid resolution in Table 1, because this did not significantly improve results for a wind direction of 270° (not shown). The simulation results are compared with measurements at the eight mast locations shown in Fig. 1.

4 Results

4.1 Comparison Between the Linear and Stress Methods

Following [Bechmann et al. \(2011\)](#), the speed-up ΔS and speed-up error R_s are used to evaluate the prediction of the mean wind speed according to

$$\Delta S = \frac{U(z) - U_{RS}(z)}{U_{RS}(z)}, \tag{10}$$

and

$$R_s = 100 (\Delta S_s - \Delta S_m), \tag{11}$$

where $U(z)$ is the time-averaged wind speed at a height z above ground level (a.g.l.), and $U_{RS}(z)$ is the time-averaged wind speed at a reference site M0 or M9 (inlet boundary). The subscript s and m denote the simulated and measured variables, respectively. The speed-up, which is a normalized wind-speed deficit used widely for the evaluation of numerical models, indicates the departure from the inflow speed at the same height a.g.l. Note that a negative speed-up does not necessarily imply a recirculation flow.

Both immersed-boundary methods are tested using the coarse-grid resolution with the same model configurations as the LASD-dx2m case. Comparison of the speed-up for the 270° flow direction shows that the linear method gives results inferior to the stress method, particularly near the near-surface region (Fig. 2), with the greatest differences occurring in regions close to the surface at the M2 and M7 sites, where a small recirculation exists. Table 2 shows the mean absolute speed-up errors for the four wind directions, with the numbers in parentheses showing the errors for the stress method. Overall, the stress method performs better than the linear method near the surface, with a mean absolute error of 13% for the stress method and 20% for the linear method at 2 m a.g.l. At 5 m a.g.l., although both methods yield a similar speed-up, with a mean absolute error of 10% for the stress method and 12% for the linear method, the actual wind speeds differ greatly. Since the wind speeds shown here are

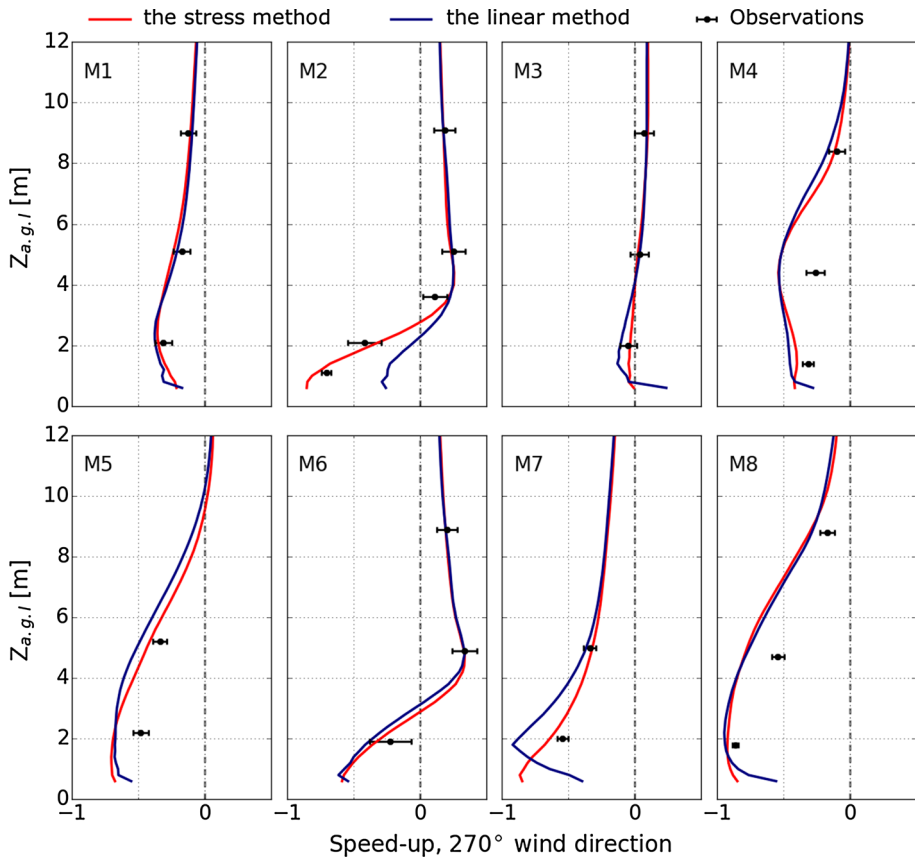


Fig. 2 Vertical profiles of speed-up at the eight mast locations for the 270° wind-direction case

Table 2 Comparison of mean absolute speed-up error R_S (%) between the two immersed-boundary methods for four wind directions at eight sites (M1–M8)

Wind direction (°)	2 m a.g.l.	5 m a.g.l.	Average of 2 and 5 m a.g.l.
270	17.9 (7.9)	9.1 (9.0)	13.5 (8.5)
255	20.9 (13.6)	6.2 (3.9)	13.6 (8.7)
239	19.0 (16.2)	14.3 (11.4)	16.6 (13.8)
90	21.6 (16.1)	16.9 (16.6)	19.3 (16.4)

The numbers in parentheses represent the errors for the stress method

normalized, the actual wind speeds for the linear method are much smaller than those for the stress method. Therefore, the stress method is used for the remaining simulations.

4.2 Overall Performance of the Simulation of Speed-Up

There is generally good agreement in the simulation of speed-up between simulations and observations, with the best performance by the LASD-dx1m run (coefficient of determination

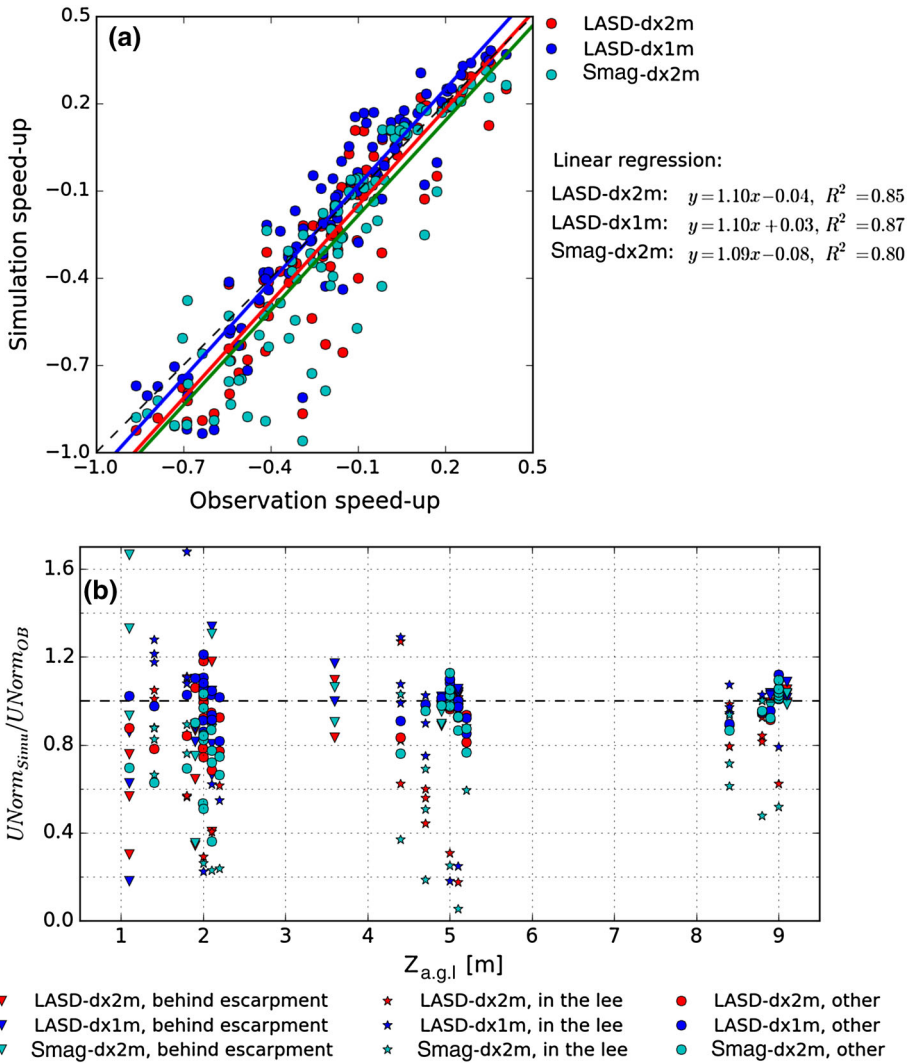


Fig. 3 Overall performance of the simulations from the four wind directions at the eight mast locations, **a** Scatterplot of simulated and observed speed-up, the *solid lines* are generated from the linear regression, **b** ratio of simulations to observations for the normalized wind speed. Different *colours* denote different simulation sets, and different *markers* different observation locations

$R^2 = 0.87$) and the worst performance by the Smag-dx2m run ($R^2 = 0.80$) (Fig. 3a). The LASD-dx2m run tends to underpredict the speed-up. All three runs perform better in the high speed-up ranges (approximately $\Delta S \geq 0.1$) than in the low speed-up ranges (approximately $\Delta S < 0.1$). Linear regression indicates that all the simulations tend to underpredict the speed-up in the low ranges where recirculation flows usually develop, suggesting the simulation of excess recirculation.

To further investigate the overall model performance in simulating recirculation, we first separate the data into three groups: behind the escarpment, on the lee side of the hill, and at the remaining locations, and then calculate the ratio of the simulated and observed wind

Table 3 Mean absolute speed-up error R_S (%) for our simulations and those reported in the literature

	270°	255°	239°	90°	Four directions averaged
LASD-dx2m	8.5	8.7	13.8	16.4	11.9
LASD-dx1m	6.3	6.4	9.4	13.1	8.8
Smag-dx2m	14.9	10.2	14.4	22.0	15.4
Bechmann et al. (2011)	–	–	–	–	16.0
Diebold et al. (2013)	12.1	5.9	7.1	24.0	12.3
Conan et al. (2016)	11	–	–	–	–

All results are obtained with LES modelling

speeds (Fig. 3b), with the normalized wind speed $UNorm$ defined as $U(z)/U_{RS}(z)$. Note that in Fig. 3b, the discrepancy is amplified for measured very small wind speeds. The greatest differences in the speed-up occur behind the escarpment and on the lee side of the hill, especially in the near-surface region where recirculation flows are most likely to occur (Fig. 3b). Almost all the simulations tend to underestimate wind speeds on the lee side of the hill. Behind the escarpment, complex flow patterns occur near the surface (below 5 m a.g.l.), where previous studies report difficulties in obtaining accurate flow simulations (Prospathopoulos et al. 2012; Vuorinen et al. 2015). For locations apart from the lee side and behind the escarpment, the LASD model simulates the speed-up fairly well, whereas the Smagorinsky model underpredicts the speed-up, particularly below 2 m a.g.l. Generally, our simulations indicate that the LASD-dx1m run performs reasonably well behind the escarpment region, on the lee side, as well as the other regions.

The mean absolute speed-up errors are summarized in Table 3 for a complete evaluation of the model performance. Here, we only present the results at 2 and 5 m a.g.l. to compare with previous studies (see Bechmann et al. 2011 for details). In Table 3, the error reported by Bechmann et al. (2011) is averaged from six blind LES results. For the LES of Diebold et al. (2013), the LASD model with a pseudo-spectral code was used, while Conan et al. (2016) deployed an unstructured CFD code (e.g., OpenFOAM) with a TKE-based SGS model. Table 3 shows that the LASD-dx1m run has the smallest mean absolute speed-up error (9%), while the Smag-dx2m run has the largest error (15%), indicating that the dynamic SGS model with a fine grid resolution substantially improves the results (Table 3). Smaller or comparable errors with other studies are found here even though our grid resolution is coarser. For example, a grid resolution of $dx = dy = dz = 1$ m was used by Diebold et al. (2013), and a much finer grid resolution of $dx \approx 0.3$ m and $dz \approx 0.15$ in the escarpment region was used by Conan et al. (2016).

4.3 Recirculation Flows Around the Escarpment

As the simulated flow patterns in the 270°, 255° and 239° flow-direction cases are quite similar, we analyze the 270° direction, which has been numerically studied extensively (Vuorinen et al. 2015; Conan et al. 2016), with wind-tunnel experiments (Yeow et al. 2015; Conan et al. 2016), and lidar field observations (Lange et al. 2016).

Figure 4 compares the speed-up profiles along line B shown in Fig. 1 at 2 and 5 m a.g.l. Whereas the LASD-dx1m case reproduces the horizontal speed-up well, large discrepancies exist between both the LASD-dx2m and Smag-dx2m simulations, and observations on the lee

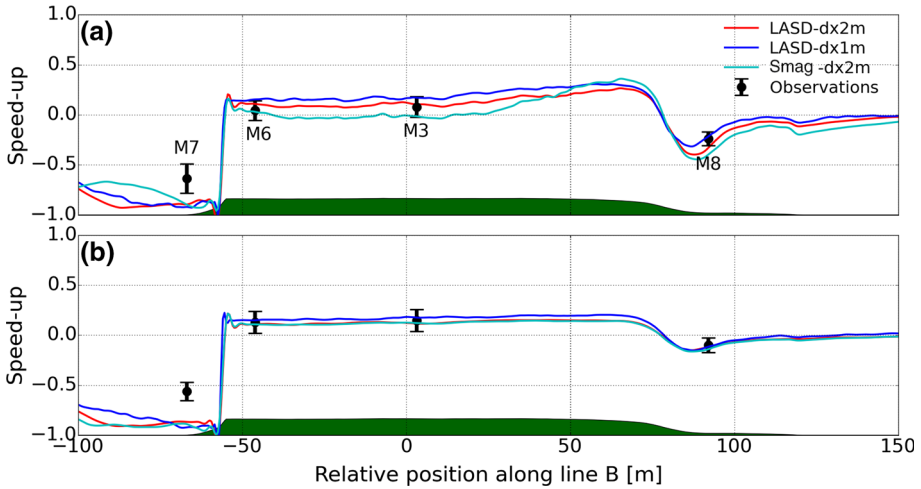


Fig. 4 Speed-up profiles at, **a** 2 m, and **b** 5 m above ground level along line B for the 270° wind-direction case

side of the hill and behind the escarpment, which are largely due to the inaccurate simulation of the recirculation. Flow deceleration occurs upstream of the escarpment (near the M7 site) as indicated by all three runs, the observed vertical profiles of the speed-up at the M1 and M7 sites (Figs. 4, 5), and by the many previous numerical studies (Lopes et al. 2007; Chow and Street 2009; Diebold et al. 2013), wind-tunnel experiments (Yeow et al. 2015), and even linearized analytical models (Bechmann et al. 2011). The vertical speed-up profiles presented in Fig. 5, together with the observations, indicate that the LASD-dx2m run performs better than the Smag-dx2 run.

It is a challenging task to correctly simulate the near-surface flow behind the escarpment, where the most divergent results from the three runs are detected (see the M6 site in Fig. 4a, and the M2 site in Fig. 5). A substantial speed-up reduction behind the escarpment is simulated well by all three runs (Fig. 4a), which is attributable to the existence of recirculation. The averaged streamwise velocity component (Fig. 6) indicates a slight recirculation from all three runs, consistent with the speed-up profiles (Fig. 4a). Note that, because the recirculation zone is so small, it has a negligible impact on the flow at 5 m a.g.l., resulting in a nearly identical speed-up for the three runs. The small recirculation region explains why previous simulations usually overestimate the speed-up at 2 m a.g.l. at the M6 site (Prospathopoulos et al. 2012; Vuorinen et al. 2015; Yeow et al. 2015; Cavar et al. 2016; Conan et al. 2016). Our simulated recirculation is supported by lidar observations indicating a recirculation height of about 2 m (see Lange et al. 2016).

The simulated sizes and positions of the recirculation depends on the nature of the SGS model, as well as the grid resolution. Recirculation is suppressed slightly in the vertical direction by the Smagorinsky model, tending to elongate along the downwind direction, resulting in a longer distance for flow recovery, which explains the small underestimation of speed-up at 2 m a.g.l. at the M3 site. However, recirculation is clearly present in the results of the LASD model, with varying recirculation size and position suggesting the influence of the grid resolution. A relatively smaller recirculation closer to the escarpment is reproduced by the LASD-dx1m run compared with the LASD-dx2m run. Note that the recirculation behind the escarpment is greatly dependent on the choice of the Smagorinsky coefficient for the

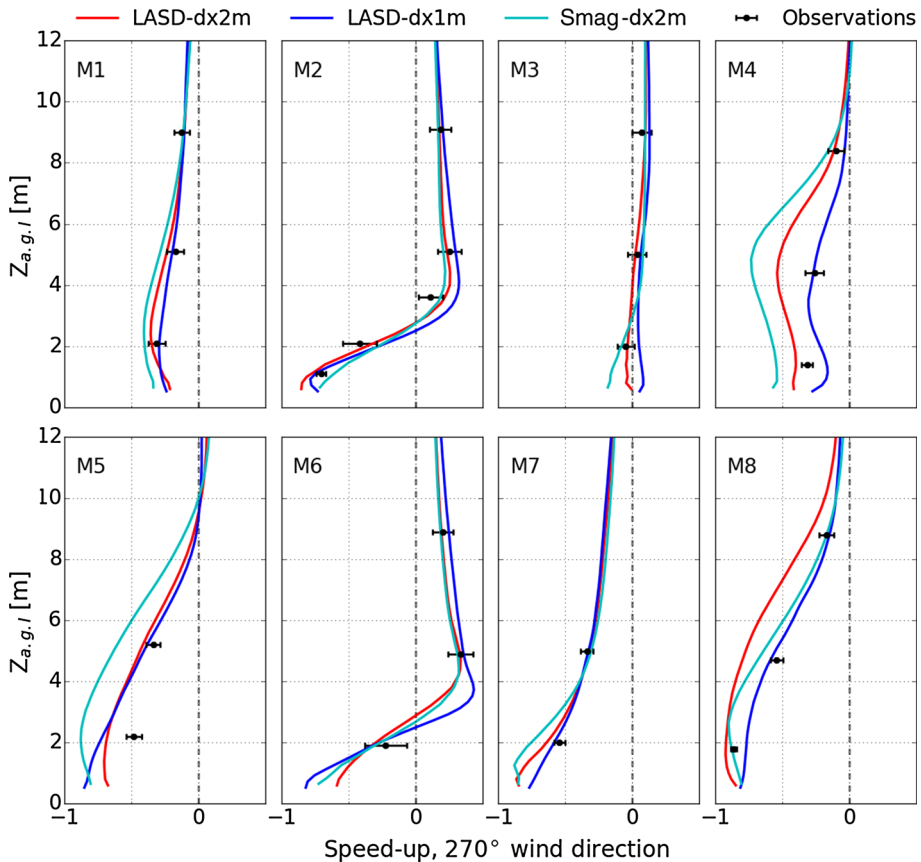


Fig. 5 Vertical profiles of speed-up at the eight mast locations for the 270° wind-direction case

Smagorinsky runs. Simulations with the default value of $C_s \Delta = 0.25$ indicate a substantially suppressed recirculation, which is absent in the mean velocity field (not shown).

To further investigate the impact of the SGS model, we depict the time-averaged Smagorinsky coefficient in Fig. 7. Clearly, the coefficient from the LASD model decreases as the surface is approached, with a particularly small coefficient over the escarpment where a large strain rate is found. The coefficient for the LASD-dx1m run is slightly larger than that for the LASD-dx2m run, suggesting a dependence on the grid resolution. Figure 7 also demonstrates a Smagorinsky coefficient of 0.15 near the recirculation zone behind the escarpment consistent with the value in the Smag-dx2m run, which reproduces a similar recirculation in this region. Hence, the recirculation flow is sensitive to the Smagorinsky coefficient, with a large coefficient tending to suppress recirculation by dissipating resolved energy at the sub-grid scale. The relatively larger coefficient at the M6 site for the LASD-dx2m run partially explains the small shift of the recirculation zone compared with the Smag-dx2m run.

4.4 Recirculation on the Lee Side of the Hill

Generally, the two SGS models reproduce different recirculation patterns on the lee side of the hill (Fig. 6). The Smagorinsky model tends to suppress the recirculation in the verti-

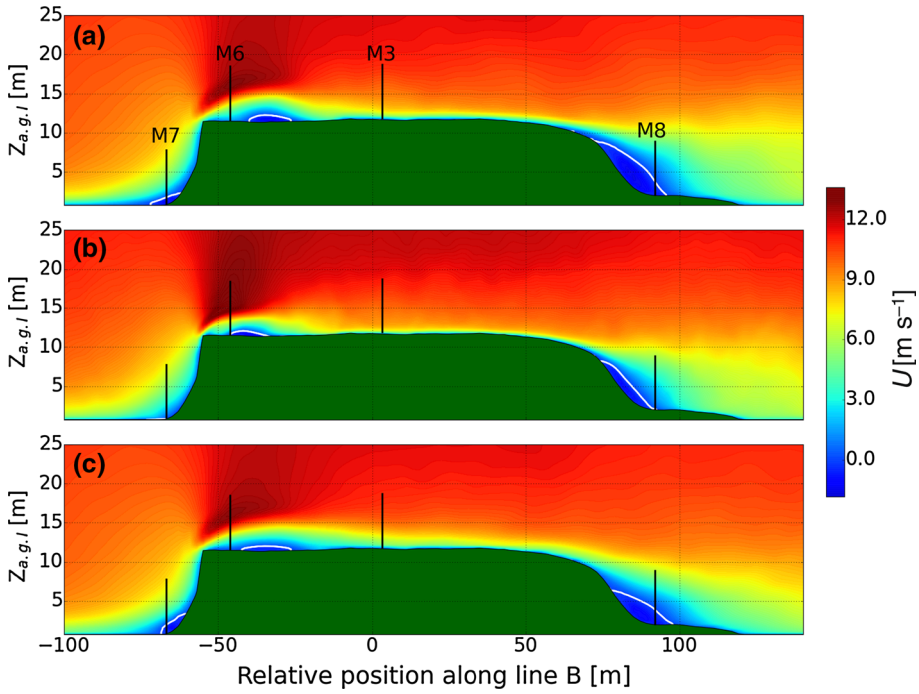


Fig. 6 Vertical cross-section of the mean streamwise velocity component along line B for the 270° wind-direction case, **a** LASD-dx2m, **b** LASD-dx1m, and **c** Smag-dx2m. Vertical black lines denote the locations of masts. The zero streamlines are marked with white lines

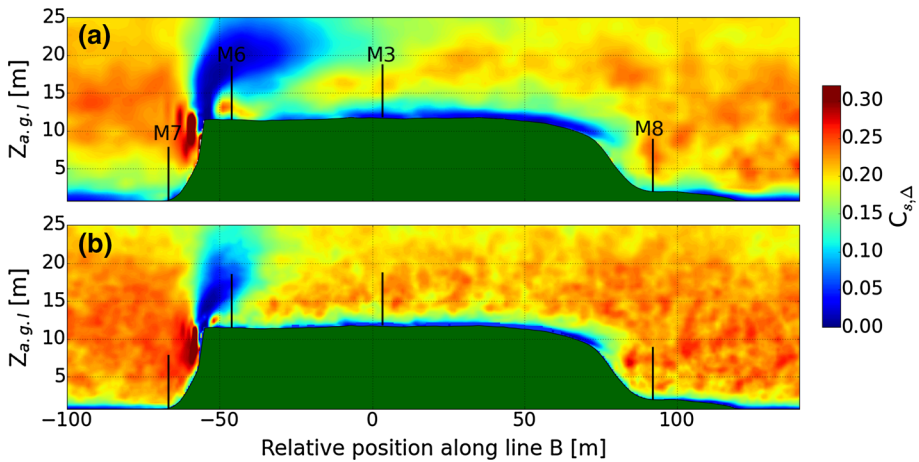


Fig. 7 The mean Smagorinsky coefficient $C_{s,\Delta}$ for the 270° wind direction case along line B. **a** LASD-dx2m, **b** LASD-dx1m

cal direction, resulting in an elongated recirculation downstream (see also the recirculation behind the escarpment). The LASD model predicts a deeper recirculation consistent with Kirkil et al. (2012), with the LASD-dx1m run predicting a relatively smaller recirculation zone than found in the LASD-dx2m run (see Fig. 6a, b). Although the flow pattern is sim-

ulated differently on the lee side of the hill by the LASD-dx1m and Smag-dx2m runs, the vertical profiles of the speed-up at the M8 site both agree well with observations (see the M8 panel in Fig. 5). From the overall performances on the lee side of the hill (Fig. 3b) and the smaller mean speed-up errors (Table 3), we find that the LASD-dx1m run generates a more reliable flow pattern than the other runs, but with a slight underestimation of the size of the recirculation at the M8 site (Fig. 5), where one expects a deep, narrow recirculation. The vertical suppression of the recirculation on the lee side of the hill by the Smag-dx2m run may result from the relatively large Smagorinsky coefficient in the upper portion of the recirculation zone (see Fig. 7a). Tests with a larger coefficient ($C_{s,\Delta} = 0.25$) for the Smag-dx2m run result in the further suppression of the recirculation in the vertical direction, which is consistent with previous studies. For example, Allen and Brown (2002) reported a depressed recirculation on the lee side of a two-dimensional hill when using the Smagorinsky model. Chow and Street (2009) found that the 1.5-order TKE model underestimates recirculation, and overpredicts the speed-up on the lee side of the Askervein hill.

Note that the flow characteristics for the 90° direction differ from the other three wind directions. The sudden decrease in the speed-up downwind from the escarpment is substantially underestimated by all three runs, leading to the largest mean speed-up error among the four wind directions (Table 3). Diebold et al. (2013) also found the largest error for this wind direction when using the LASD model, and attributed this error to the difference in surface roughness between the land and water. However, it may also be caused by the wall model used in the stress method, as the nature of the SGS model may also play a role here. However, further confirmation is required.

4.5 Mean Prediction of Turbulent Kinetic Energy

To evaluate the production of TKE, the TKE increase ΔK and TKE error R_{TKE} are defined as

$$\Delta K = \frac{K(z) - K_{RS}(z)}{U_{RS}^2(z)} \tag{12}$$

and

$$R_{TKE} = 100 \frac{(I_s - I_{0s}) - (I_m - I_{0m})}{I_{0m}}, \tag{13}$$

respectively, where $K(z)$ is the TKE at height z , $K_{RS}(z)$ is the TKE at a reference site (inlet boundary), and $I = \sqrt{K}/U_{RS}$. Note that, since both the LASD and Smagorinsky models do not provide the unresolved TKE explicitly, we use the SGS stresses to estimate the unresolved TKE (Mason and Callen 1986). Hence, the total TKE is

$$K_{total} = 0.5 \left[\left(\widehat{u'u'} + |\tau_{11}| \right) \right] + \left(\widehat{v'v'} + |\tau_{22}| \right) + \left(\widehat{w'w'} + |\tau_{33}| \right), \tag{14}$$

where u' is defined as the departure of instantaneous \tilde{u} from its time-averaged value (with the same definition for v' and w'), and the overbar symbol ($\widehat{\quad}$) denotes time-averaging.

The overall performance of the four direction cases is shown in Fig. 8. With the exception of the region behind the escarpment where the TKE increase is greatly underestimated, all runs simulate an accurate TKE increase despite the generally superior performance of the LASD-dx1m run compared with the LASD-dx2m and Smag-dx2m runs. Similar predictions of the TKE increase for the LASD-dx2m and Smag-dx2m runs are attributable to the similar magnitude of the Smagorinsky coefficient behind the escarpment. The mean absolute TKE errors indicate that the overall TKE increase is comparable with previous studies (Table 4). The TKE error for the 90° case confirms that the primary error source is the recirculation

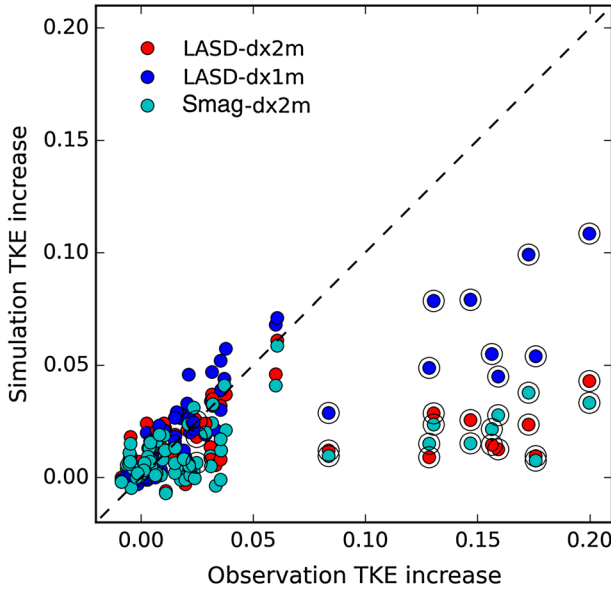


Fig. 8 Scatter plot of simulated and observed TKE increase from LASD-dx2m and LASD-dx2m. The four wind-direction cases at eight mast locations are included. The M2 and M6 sites for the 270°, 255° and 239° wind directions near the surface (below 4 m a.g.l.) are marked with *black circles*

Table 4 Mean absolute TKE errors

	270°	255°	239°	90°	Four directions averaged
LASD-dx1m	35.8	34.0	38.6	8.1	29.1
LASD-dx2m	52.7	55.5	56.7	16.7	45.4
Smag-dx2m	56.9	58.3	61.7	22.2	49.8
Bechmann et al. (2011) LES	–	–	–	–	35.9
Yeow et al. (2015) wind tunnel	56.3	–	–	–	–
Conan et al. (2016) LES	19	–	–	–	–

behind the escarpment, since errors for the 90° case without a recirculation are smaller than the other three wind-direction cases with recirculation behind the escarpment (see Table 4; Fig. 8).

To further evaluate model performance in the simulation of TKE, we analyze the results of the 270° wind-direction case. The Smag-dx2m run provides a similar TKE field to the LASD-dx2m run, but with a smaller value above the recirculation (Fig. 9). The size of the elevated TKE region behind the escarpment for the Smag-dx2m run is larger than that for the LASD-dx2m run, corresponding to the mean velocity field (Fig. 6). Note that the TKE fields are different from the two LASD model runs, with the finer grid resolution resulting in larger TKE values than the case of the coarser resolution, suggesting the underestimation of the unresolved part of the TKE by Eq. 14. Another notable feature in Fig. 9 is the closer location of the peak value of TKE to the escarpment for high-resolution runs, as indicated more clearly in the horizontal profiles of TKE increase in Fig. 10.

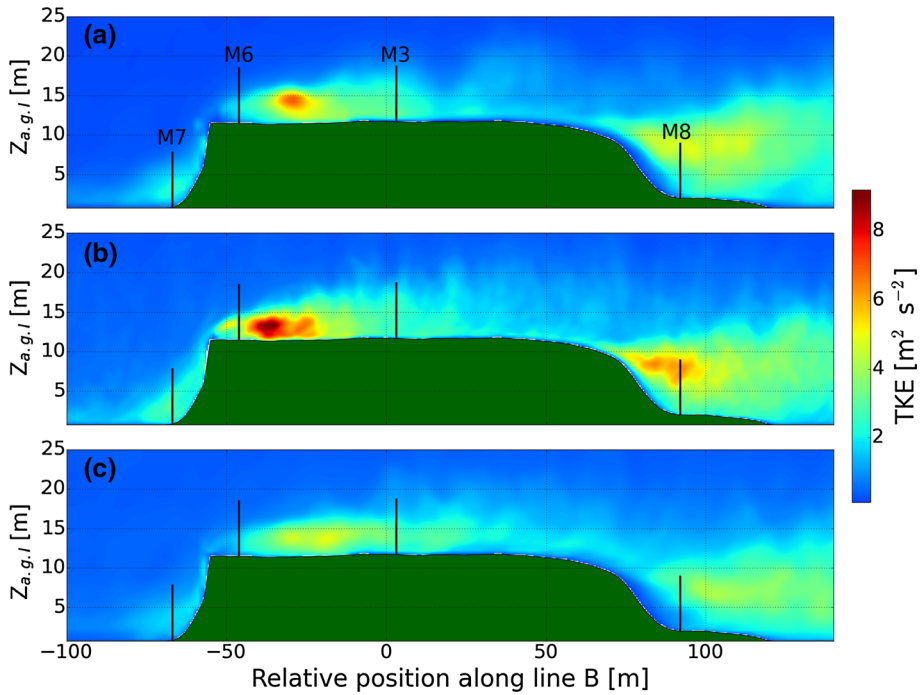


Fig. 9 Vertical cross-section of mean resolved TKE along line B for the 270° wind-direction case, **a** LASD-dx2m, **b** LASD-dx1m, and **c** Smag-dx2m. Vertical black lines denote the locations of masts

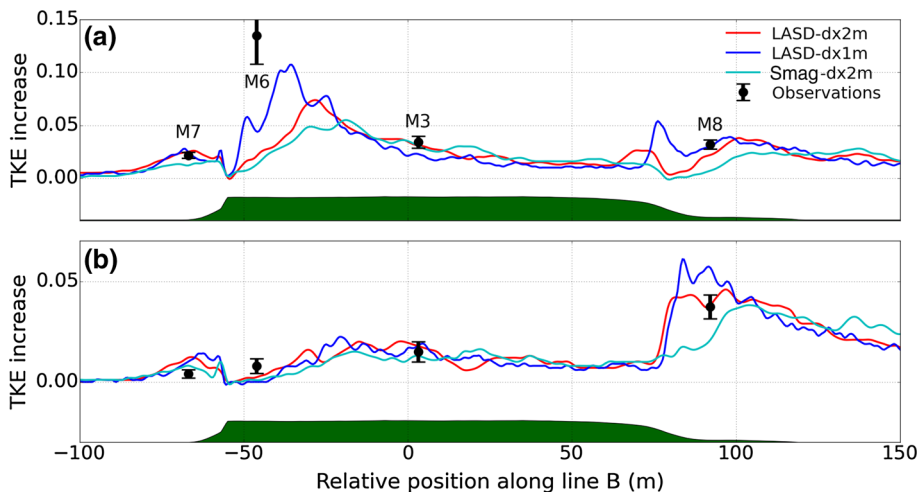


Fig. 10 Horizontal profiles of the TKE increase at, **a** 2 m, and **b** 5 m above ground level along line B for the 270° wind-direction case

As shown in Fig. 10, the TKE increase is relatively well simulated, except for the near-surface region behind the escarpment, where the TKE is underestimated, consistent with previous results from both RANS and LES models (Prospathopoulos et al. 2012; Jafari et al. 2012; Conan et al. 2016; Cavar et al. 2016). In our simulations, although the speed-up at the

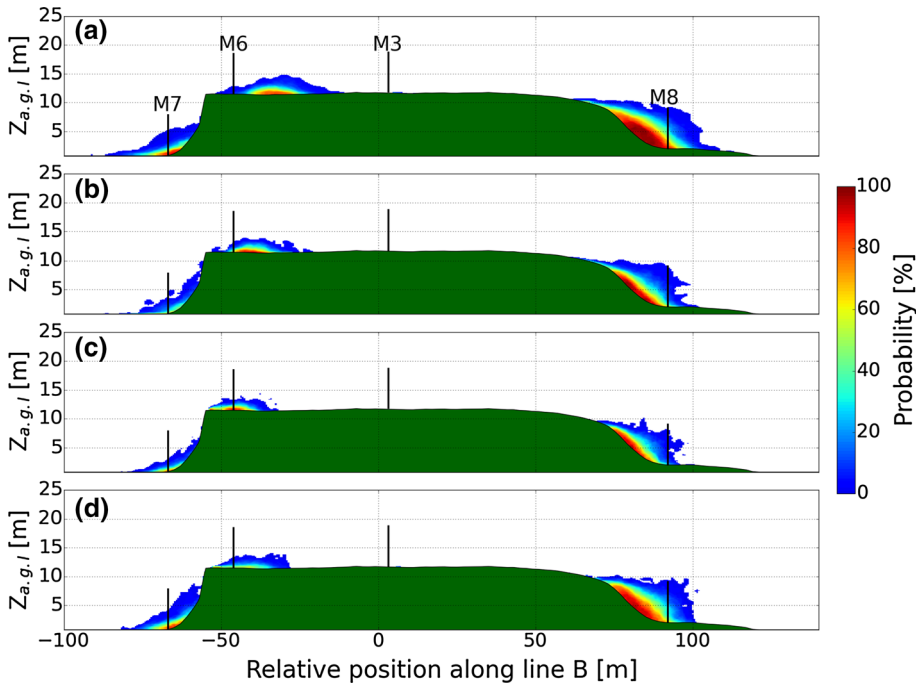


Fig. 11 Probability of occurrence of the instantaneous negative streamwise velocity component at the plane along line B. **a** LASD-dx2m, **b** LASD-dx1m, **c** test 1 ($dx = dy = 0.5$ m, $dz = 0.25$ m), **d** test 2 ($dx = dy = 0.5$ m, $dz = 0.5$ m)

M6 site is predicted well, it is still difficult to predict an accurate magnitude of the TKE. We also note that the peak value of the TKE increase at 2 m a.g.l. produced by the LASD-dx1m run is close to the observations (at the M6 site), with its location shifting towards the escarpment. This shows that the grid resolution of LASD-dx1m is still insufficiently fine for capturing most of the energetic eddies being generated at the escarpment.

4.6 Grid Sensitivity of the Recirculation Flows

A further objective is the investigation of the recirculation immediately behind the escarpment, whose simulation has proven difficult in the past (see discussion above). We find that a large SGS eddy viscosity suppresses the development of recirculation in this area, resulting in an overprediction of the velocity speed-up. The grid resolution also influences the magnitude of the TKE by affecting the location and shape of the recirculation zone.

To test the sensitivity to the grid resolution, two additional simulations for the 270° wind-direction case are considered with a smaller grid spacing: one case with $dx = dy = 0.5$ m and $dz = 0.25$ m (hereafter test 1), and another case with $dx = dy = 0.5$ m and $dz = 0.5$ m (hereafter test 2). The LASD model is used in both cases, with the same domain size as the LASD-dx2m run. To save computational time, periodic horizontal boundary conditions are used instead of the turbulent inflow conditions, which is acceptable since the hill is relatively low, and the flow recovers at approximately 150 m downwind of the hill.

Figure 11 shows the probability of occurrence of an instantaneous negative streamwise velocity component on the plane along line B (see Fig. 1), together with the LASD-dx2m and LASD-dx1m simulations for comparison. Note that the LASD-dx2m run and test 2 have

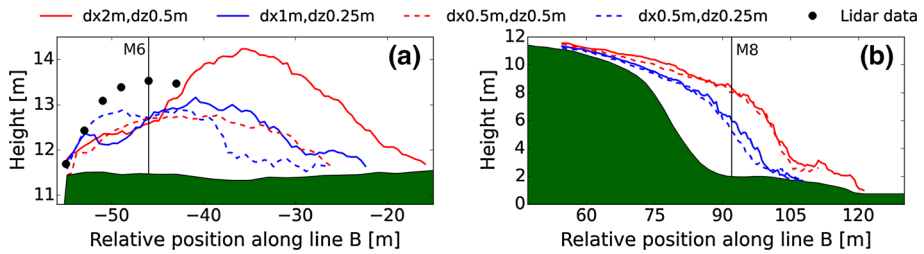


Fig. 12 Time-averaged recirculation heights with different grid resolutions, **a** just behind the escarpment, **b** on the lee side of the hill

the same vertical resolution of 0.5 m (Fig. 11a, d), and the LASD-dx1m run and test 1 have the same vertical resolution of 0.25 m (Fig. 11b, c). Figure 11 shows that the recirculation behind the escarpment is mainly controlled by the horizontal resolution. As the horizontal grid spacing decreases, the size of the recirculation behind the escarpment becomes smaller, and the centre of the recirculation zone shifts towards the escarpment. Interestingly, for the recirculation on the lee side of the hill, the vertical resolution plays a more important role than the horizontal resolution.

To give a direct comparison, we plot the recirculation size, and compare the results with the lidar measurements reported in Lange et al. (2016). The recirculation height δ is calculated using

$$\delta = \underset{z}{\operatorname{arg\,max}} \left[\frac{d\tilde{u}(z)}{dx} \right], \tag{15}$$

with the time-averaged height shown in Fig. 12. It is clear that the recirculation size behind the escarpment is overestimated by the LASD-dx2m run, while the other three simulations generally reproduce similar results. Figure 12 also confirms the tendency shown in Fig. 11 that the horizontal resolution has a significant impact on the simulation of the recirculation flow behind the escarpment, with a minor impact resulting from the vertical resolution. Although the four cases simulate different recirculation shapes, they all produce almost the same recirculation height at the M6 site, leading to a similar speed-up prediction there (Fig. 4). The recirculation on the lee side of the hill suggests the opposite conclusion: the flow is mainly affected by the vertical grid resolution instead of the horizontal resolution, which we also conclude for the flow before the escarpment (Fig. 11). The different grid-resolution dependences can be explained by the different turbulent flow structures in the two regions. Just behind the escarpment, the flow has a strong horizontal wind shear, while on the lee side of the hill, the flow has a strong vertical wind shear (Fig. 6). We also notice a similar relationship between the size of the well-resolved recirculation and the grid resolution. The ratio of the recirculation length behind the escarpment to the horizontal grid resolution is approximately 40, which is identical to the ratio of the recirculation height on the lee side to the vertical grid resolution.

5 Numerical Diffusion from the Odd-Ordered Upwind-Biased Advection-Differencing Method

It is well-known that the fifth-order upwind-biased differencing scheme for horizontal advection in the WRF model induces numerical diffusion, which is a similar feature to a SGS model

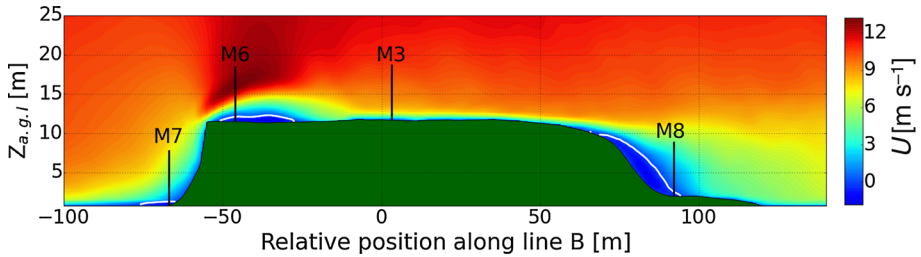


Fig. 13 Vertical cross-section of the mean streamwise velocity component along line B for the 270° wind-direction case without a SGS model. The domain configurations are the same as the LASD-dx2m run

(Kniewel et al. 2007; Kirkil et al. 2012; Talbot et al. 2012). Because of the complex non-linear interactions between numerical diffusion and SGS model near the grid spacing, it is difficult to identify the effect of numerical diffusion in the LES model. For simplicity, we deactivate the SGS models to examine the effects of numerical diffusion, which is termed implicit LES (Grinstein et al. 2007). Hence, the simulation configurations are the same as the LASD-dx2m run, except without a SGS model. Figure 13 shows the time-averaged streamwise velocity component on the vertical plane along the line B. Interestingly, the main features in the mean velocity field are similar to those from the LASD-dx2m run, despite a notable difference in the recirculation behind the escarpment. Without a relatively large SGS diffusion (see the M6 site in Fig. 7a), the recirculation elongates towards the escarpment, which is consistent with our previous analysis. For the recirculation zone on the lee side of the hill, the detachment point is slightly higher than for the LASD-dx2m run, and we note that the flow in these two regions contains many small energetic eddies (Fig. 9). Therefore, the truncation error from the odd-ordered discretization scheme alone cannot provide adequate diffusion in the recirculation region. The truncation error, however, is similar to the LASD model in the areas of low TKE.

It is worth noting that, although a similar mean velocity field is reproduced by the implicit LES with a mean absolute speed-up error of 9%, a greater discrepancy occurs in the simulation of TKE. Here, much higher TKE is generated than for the LASD-dx2m run in the recirculation region. Compared with the observations, the implicit LES approach overestimates the TKE increase at most locations with a mean absolute TKE error of 66%. Note that the simulated magnitude of TKE at the M6 site is mainly affected by the horizontal grid resolution, confirming our previous conclusion that the numerical diffusion alone is inadequate in the recirculation region. Although the interaction between the numerical diffusion and the LASD model could not be identified clearly in our results, the simulation of the recirculation is largely unaffected by the numerical diffusion when using a SGS model. Hence, the LASD model provides sufficient diffusion for the reduction of the numerical diffusion (Xie et al. 2015), especially in the recirculation region.

6 Conclusion

We incorporated the immersed-boundary methods and the LASD model into the LES module within the WRF model to investigate the flow around Bolund Hill. Good agreement between the results of the simulations and observations demonstrate the capability of our modelling system in simulating atmospheric flows with recirculation. The stress method outperforms the

linear method, and helps to generate a small recirculation zone behind the escarpment of the Bolund Hill, leading to the observed low speed-up and high TKE. Our study demonstrates that SGS models have a significant impact on the prediction of recirculation. The LASD model performs better than the Smagorinsky model over complex terrain by reproducing a reliable pattern of turbulent flow. The magnitude of the Smagorinsky coefficient significantly affects the results, especially within the small recirculation zone behind the escarpment. The shapes and locations of the recirculation zones are also influenced by the numerical grid resolution. A horizontal resolution is more important for reproducing the recirculation immediately behind the escarpment, whereas the vertical resolution is more important for the flow on the lee side of the hill. Numerical diffusion tests suggest that the discretization-truncation errors are small in the recirculation regions, where the SGS model has a significant influence, thus the accuracy of the simulations is not greatly influenced by numerical diffusion.

In general, our modelling system reproduces the recirculation reasonably well over the Bolund Hill. However, as pointed out in Sect. 4.4, the flow downstream of the escarpment for the wind direction of 90° is not well captured, for which the equilibrium wall model used in the stress method may be at fault. In future work, a more sophisticated wall model (i.e., Yang et al. 2015b) should be tested.

Acknowledgements We thank Brian Lamb, Eric Russell, Justine Missik, Zhongming Gao, and Raleigh Grysko for their comments, which greatly improved this work. We are grateful to three anonymous reviewers for their constructive suggestions, which also greatly improved the manuscript. We acknowledge support by National Science Foundation AGS under Grants #1419614. We acknowledge high-performance computing support from Yellowstone (ark:/85065/d7wd3xhc) provided by NCAR's Computational and Information Systems Laboratory, sponsored by the National Science Foundation.

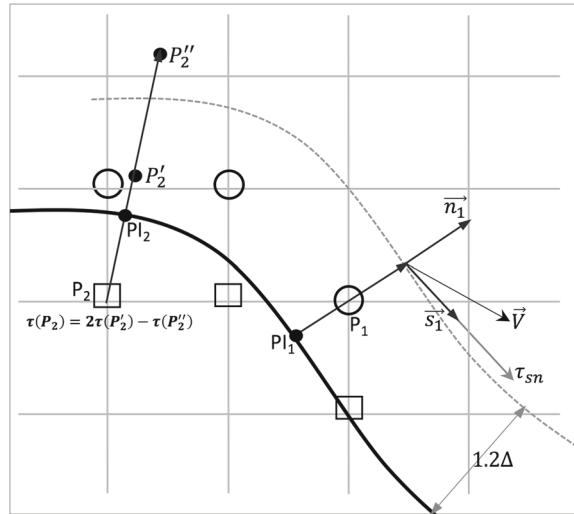
Appendix 1: Implementation of the Stress Immersed-Boundary Method

The implementation of the stress method in the LES module of the WRF model consists of four steps:

Step 1 Identify two layers of reconstruction grid nodes: one layer contains the first grid nodes immediately above the immersed surface (circles in Fig. 14), while the other layer contains the first grid nodes just below or on the immersed surface (squares in Fig. 14). The reconstruction nodes are identified by searching column-by-column along the grids of the WRF model. Also, the velocities are all set to zero at any grid nodes below the immersed surface.

Step 2 Find the surface-normal direction for each reconstruction node. In our implementation, the surface/terrain is represented at the discrete points at one-half of the grid spacing of the WRF model using a two-dimensional array $H_{i,j}$ (where i and j are the grid numbers in the horizontal directions). We first determine the closest surface point (e.g., H_{i_0,j_0}) for a chosen reconstruction node P . Then, eight surrounding surface-discrete points H_{i_0-1,j_0-1} , H_{i_0,j_0-1} , H_{i_0+1,j_0-1} , \dots , H_{i_0+1,j_0+1} are identified, and those points construct eight triangles with a shared vertex H_{i_0,j_0} . On each triangle, find an intercept point (not necessarily the projection point) with the shortest distance to P , and repeat for eight triangles to produce the intercept point PI having the shortest distance to P for all eight triangles. The direction from PI to P (or from P to PI) is assumed to be the surface-normal direction \mathbf{n} for the node P . In the case that PI coincides with P where \mathbf{n} cannot be identified, a small modification is made on H_{i_0,j_0} , and we revert back to find

Fig. 14 Schematic of the implementation of the stress method. The *solid black line* denotes the immersed surface. The *circles* are the reconstruction points of the stresses, and the *squares* are the smooth transition points. The *line through circles and squares* are in the surface-normal directions. The stresses are assumed to be constant along the surface normal direction in the layer of thickness 1.2Δ



the intercept point PI . Note that this procedure allows PI to be on the edge or vertex of the triangles.

Step 3 Specify stresses at the circled points in Fig. 14. Let P_1 denote a circled point, PI_1 denote the corresponding intercept point on the immersed surface, and \mathbf{n}_1 denote the surface-normal direction passing through P_1 . The velocity \mathbf{V} at a distance around the grid spacing from the immersed surface along \mathbf{n}_1 can be identified by a trilinear interpolant, for which we use a distance of 1.2Δ , where Δ is the grid spacing. Next, define the local spanwise direction of the flow $\mathbf{w}_1 = \mathbf{n}_1 \times \mathbf{V} / |\mathbf{V}|$ and the streamwise direction $\mathbf{s}_1 = \mathbf{w}_1 \times \mathbf{n}_1$. In this local coordinate system defined by \mathbf{s}_1 , \mathbf{w}_1 , and \mathbf{n}_1 , the tangential velocity component is calculated as $V_t = \mathbf{V} \cdot \mathbf{s}_1$. The surface shear stress is parametrized as

$$\tau_{surf} = \tau_{sn} = - \left[\frac{k V_t}{\ln \left(1 + \frac{1.2\Delta}{z_0} \right)} \right]^2, \tag{16}$$

where z_0 is the roughness length and $k = 0.4$ is the von Kármán constant. Finally, the local shear stress is transformed to the grid stress of the WRF model using $\tau_{ij}(P_1) = a_{is} a_{jn} \tau_{sn}$, where the a_{ij} is the direction cosine between the x_i axis of the WRF model and the local x_j axis.

Step 4 Specify stresses at square points using extrapolation. Let P_2 denote a square point, PI_2 denote the corresponding intercept point on the immersed surface, d_2 denote the distance from P_2 to PI_2 , and \mathbf{n}_2 denote the surface-normal direction passing through P_2 . Two points in the fluid along \mathbf{n}_2 are used in the extrapolation, which are defined as $P'_2 = P_2 + h\mathbf{n}_2$ and $P''_2 = P_2 + 2h\mathbf{n}_2$, where $h = 1.1\Delta$. If $1.1\Delta < d_2$ (P'_2 is below the immersed surface), then $h = d_2 + 0.3\Delta$ is used instead for calculating P'_2 and P''_2 . The stresses at P'_2 and P''_2 are identified from a trilinear interpolant, and the stresses at P_2 are then extrapolated using $\tau(P_2) = 2\tau(P'_2) - \tau(P''_2)$.

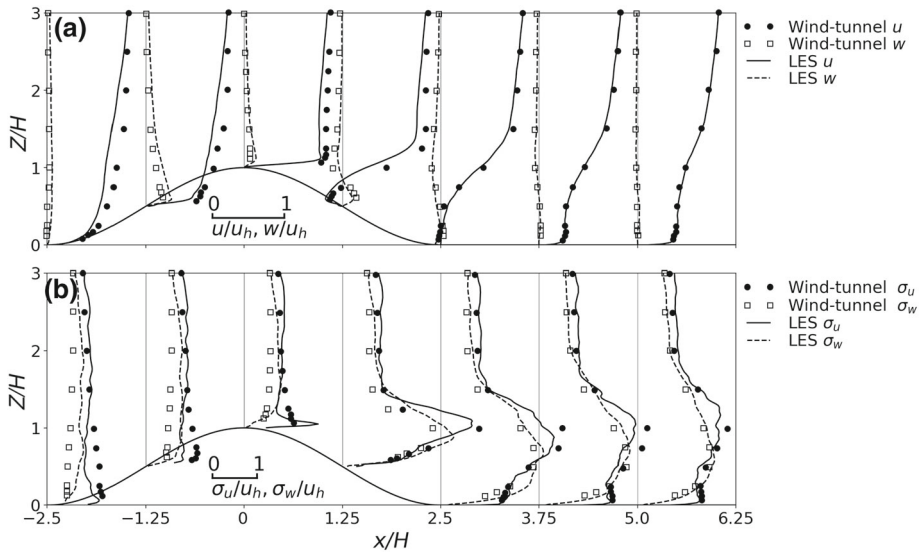


Fig. 15 LES results and wind-tunnel measurements of flows over a three-dimensional hill on the vertical slice crossing the centre of the hill. Results are normalized and averaged in time. **a** Allwise and vertical velocity components. **b** Variances of the streamwise and vertical velocity components. All LES results are normalized by $u_h = 5.1 \text{ m s}^{-1}$. Wind-tunnel data are adapted from Ishihara et al. (1999)

Appendix 2: Validation Against Wind-Tunnel Observations

We tested our modelling system against the wind-tunnel experimental data from Ishihara et al. (1999), where the height of the three-dimensional hill in the wind tunnel is described by $z(x, y) = h \cos^2\left(\frac{\pi(x^2 + y^2)^{0.5}}{2L}\right)$, with $h = 40 \text{ mm}$ and $L = 100 \text{ mm}$. The flow speed outside the boundary layer was maintained at 5.8 m s^{-1} , and the roughness length was 0.01 mm , which we also adopted. The simulation domain size is $0.76 \text{ m} \times 0.64 \text{ m} \times 0.32 \text{ m}$ in the streamwise, spanwise, and vertical directions, respectively, and the grid resolution is $dx = dy = 2.5 \text{ mm}$ and $dz = 0.8 \text{ mm}$. The upper boundary condition is set as stress-free, while the lateral boundary conditions are periodic. The simulation time is 3.5 s with a timestep of $(1/50,000) \text{ s}$. We ignore the model data during the first 1 s as a result of spin-up, and use the data during the following 2.5 s with a time interval of $(1/500) \text{ s}$ for analysis. Figure 15 shows the results of model simulations correspond well to the measurements.

References

- Abdi DS, Bitsuamlak GT (2014) Wind flow simulations on idealized and real complex terrain using various turbulence models. *Adv Eng Softw* 75:30–41
- Allen T, Brown AR (2002) Large-eddy simulation of turbulent separated flow over rough hills. *Boundary-Layer Meteorol* 102:177–198
- Bechmann A, Sørensen NN (2010) Hybrid RANS/LES method for wind flow over complex terrain. *Wind Energy* 13:36–50
- Bechmann A, Sørensen NN, Berg J, Mann J, Rethore PE (2011) The Bolund experiment, part II: blind comparison of microscale flow models. *Boundary-Layer Meteorol* 141:245–271

- Berg J, Mann J, Bechmann A, Courtney MS, Jorgensen HE (2011) The Bolund experiment, part I: flow over a steep, three-dimensional hill. *Boundary-Layer Meteorol* 141:219–243
- Bou-Zeid E, Meneveau C, Parlange M (2005) A scale-dependent Lagrangian dynamic model for large eddy simulation of complex turbulent flows. *Phys Fluids* 17:025105
- Bou-Zeid E, Overney J, Rogers BD (2009) The effects of building representation and clustering in large-eddy simulations of flows in urban canopies. *Boundary-Layer Meteorol* 132:415–436
- Castro FA, Palma JMLM, Lopes AS (2003) Simulation of the Askervein flow. Part 1: Reynolds averaged Navier–Stokes equations ($k - \epsilon$ turbulence model). *Boundary-Layer Meteorol* 107:501–530
- Cavar D, Réthoré P-E, Bechmann A, Sørensen NN, Martínez B, Zahle F, Berg J, Kelly MC (2016) Comparison of OpenFOAM and EllipSys3D for neutral atmospheric flow over complex terrain. *Wind Energy Sci* 1:55–70
- Chester S, Meneveau C, Parlange MB (2007) Modeling turbulent flow over fractal trees with renormalized numerical simulation. *J Comput Phys* 225:427–448
- Chow FK, Moin P (2003) A further study of numerical errors in large-eddy simulations. *J Comput Phys* 184:366–380
- Chow FK, Street RL (2009) Evaluation of turbulence closure models for large-eddy simulation over complex terrain: flow over Askervein hill. *J Appl Meteor Climatol* 48:1050–1065
- Conan B, Chaudhari A, Aubrun S, van Beeck J, Hämäläinen J, Hellsten A (2016) Experimental and numerical modelling of flow over complex terrain: the Bolund hill. *Boundary-Layer Meteorol* 158:183–208
- Deardorff JW (1980) Stratocumulus-capped mixed layers derived from a three-dimensional model. *Boundary-Layer Meteorol* 18:495–527
- Diebold M, Higgins C, Fang J, Bechmann A, Parlange MB (2013) Flow over hills: a large-eddy simulation of the Bolund case. *Boundary-Layer Meteorol* 148:177–194
- Ding L, Street RL (2003) Numerical study of the wake structure behind a three-dimensional hill. *J Atmos Sci* 60:1678–1690
- Grinstein FF, Margolin LG, Rider WJ (eds) (2007) *Implicit large eddy simulation: computing turbulent fluid dynamics*. Cambridge University Press, Cambridge
- Ishihara T, Hibi K, Oikawa S (1999) A wind tunnel study of turbulent flow over a three-dimensional steep hill. *J Wind Eng Ind Aerodyn* 83:95–107
- Jafari S, Chokani N, Abhari RS (2012) An immersed boundary method for simulation of wind flow over complex terrain. *J Sol Energy Eng* 134:011006
- Kim HG, Patel VC (2000) Test of turbulence models for wind flow over terrain with separation and recirculation. *Boundary-Layer Meteorol* 94:5–21
- Kirkil G, Mirocha J, Bou-Zeid E, Chow FK, Kosović B (2012) Implementation and evaluation of dynamic subfilter-scale stress models for large-eddy simulation using WRF. *Mon Weather Rev* 140:266–284
- Klemp JB, Skamarock WC, Fuhrer O (2003) Numerical consistency of metric terms in terrain-following coordinates. *Mon Weather Rev* 131:1229–1239
- Kniewel JC, Bryan GH, Hacker JP (2007) Explicit numerical diffusion in the WRF model. *Mon Weather Rev* 135:3808–3824
- Lange J, Mann J, Angelou N, Berg J, Sjöholm M, Mikkelsen T (2016) Variations of the wake height over the Bolund escarpment measured by a scanning lidar. *Boundary-Layer Meteorol* 159:147–159
- Lateb M, Meroney RN, Yataghene M, Fellouah H, Saleh F, Boufadel MC (2016) On the use of numerical modelling for near-field pollutant dispersion in urban environments—a review. *Environ Pollut* 208:271–283
- Lopes AS, Palma JMLM, Castro FA (2007) Simulation of the Askervein flow. Part 2: large-eddy simulations. *Boundary-Layer Meteorol* 125:85–108
- Lund TS, Wu X, Squires KD (1998) Generation of turbulent Inflow data for spatially-developing boundary layer simulations. *J Comput Phys* 140:233–258
- Lundquist KA, Chow FK, Lundquist JK (2010) An immersed boundary method for the weather research and forecasting model. *Mon Weather Rev* 138:796–817
- Lundquist KA, Chow FK, Lundquist JK (2012) An immersed boundary method enabling large-eddy simulations of flow over complex terrain in the WRF model. *Mon Weather Rev* 140:3936–3955
- Mason PJ, Callen NS (1986) On the magnitude of the subgrid-scale eddy coefficient in large-eddy simulations of turbulent channel flow. *J Fluid Mech* 162:439–462
- Mirocha J, Kirkil G, Bou-Zeid E, Chow FK, Kosović B (2013) Transition and equilibration of neutral atmospheric boundary layer flow in one-way nested large-eddy simulations using the weather research and forecasting model. *Mon Weather Rev* 141:918–940
- Mirocha J, Kosović B, Kirkil G (2014) Resolved turbulence characteristics in large-eddy simulations nested within mesoscale simulations using the weather research and forecasting model. *Mon Weather Rev* 142:806–831

- Mirocha JD, Lundquist JK, Kosović B (2010) Implementation of a nonlinear subfilter turbulence stress model for large-eddy simulation in the advanced research WRF model. *Mon Weather Rev* 138:4212–4228
- Mittal R, Dong H, Bozkurtas M, Najjar FM, Vargas A, von Loebbecke A (2008) A versatile sharp interface immersed boundary method for incompressible flows with complex boundaries. *J Comput Phys* 227:4825–4852
- Mittal R, Iaccarino G (2005) Immersed boundary methods. *Annu Rev Fluid Mech* 37:239–261
- Moeng C-H, Dudhia J, Klemp J, Sullivan P (2007) Examining two-way grid nesting for large eddy simulation of the PBL using the WRF model. *Mon Weather Rev* 135:2295–2311
- Mohd-Yusof J (1997) Combined immersed-boundary/B-spline methods for simulations of flow in complex geometries. *Annual Research Briefs, Center for Turbulence Research, NASA Ames/Stanford Univ* 317–327
- Peskin CS (1972) Flow patterns around heart valves: a numerical method. *J Comput Phys* 10:252–271
- Porté-Agel F, Meneveau C, Parlange MB (2000) A scale-dependent dynamic model for large-eddy simulation: application to a neutral atmospheric boundary layer. *J Fluid Mech* 415:261–284
- Prospathopoulos JM, Politis ES, Chaviaropoulos PK (2012) Application of a 3D RANS solver on the complex hill of Bolund and assessment of the wind flow predictions. *J Wind Eng Ind Aerodyn* 107–108:149–159
- Sadique J, Yang XIA, Meneveau C, Mittal R (2017) Aerodynamic properties of rough surfaces with high aspect-ratio roughness elements: effect of aspect ratio and arrangements. *Boundary-Layer Meteorol* 163:203–224
- Senocak I, Ackerman AS, Stevens DE, Mansour NN (2004) Topography modeling in atmospheric flows using the immersed boundary method. *Annual Research Briefs, Center for Turbulence Research, NASA Ames/Stanford Univ* 331–341
- Simpson CC, Sharples JJ, Evans JP, McCabe MF (2013) Large eddy simulation of atypical wildland fire spread on leeward slopes. *Int J Wild Fire* 22:599–614
- Skamarock W, Klemp J, Dudhia J, Gill D, Barker D, Duda M, Huang X, Wang W, Powers J (2008) A description of the advanced research WRF version 3. NCAR, Boulder
- Smagorinsky J (1963) General circulation experiments with the primitive equations. I. The basic experiment. *Mon Weather Rev* 91:99–164
- Talbot C, Bou-Zeid E, Smith J (2012) Nested mesoscale large-eddy simulations with WRF: performance in real test cases. *J Hydrometeorol* 13:1421–1441
- Tseng Y-H, Meneveau C, Parlange MB (2006) Modeling flow around bluff bodies and predicting urban dispersion using large eddy simulation. *Environ Sci Technol* 40:2653–2662
- Udina M, Sun J, Kosović B, Soler MR (2016) Exploring vertical turbulence structure in neutrally and stably stratified flows using the weather research and forecasting-large-eddy simulation (WRF-LES) model. *Boundary-Layer Meteorol* 161:355–374
- Vuorinen V, Chaudhari A, Keskinen JP (2015) Large-eddy simulation in a complex hill terrain enabled by a compact fractional step OpenFOAM® solver. *Adv Eng Softw* 79:70–80
- Wan F, Porté-Agel F (2011) Large-eddy simulation of stably-stratified flow over a steep hill. *Boundary-Layer Meteorol* 138:367–384
- Xie S, Archer C (2015) Self-similarity and turbulence characteristics of wind turbine wakes via large-eddy simulation. *Wind Energy* 18:1815–1838
- Xie S, Ghaisas N, Archer CL (2015) Sensitivity issues in finite-difference large-eddy simulations of the atmospheric boundary layer with dynamic subgrid-scale models. *Boundary-Layer Meteorol* 157:421–445
- Yang X, Howard KB, Guala M (2015a) Effects of a three-dimensional hill on the wake characteristics of a model wind turbine. *Phys Fluids* 27:025103
- Yang XIA, Sadique J, Mittal R, Meneveau C (2015b) Integral wall model for large eddy simulations of wall-bounded turbulent flows. *Phys Fluids* 27:025112–33
- Yeow TS, Cuerva-Tejero A, Perez-Alvarez J (2015) Reproducing the Bolund experiment in wind tunnel. *Wind Energy* 18:153–169
- Zhang N, Wang X, Peng Z (2013) Large-eddy simulation of mesoscale circulations forced by inhomogeneous urban heat island. *Boundary-Layer Meteorol* 151:179–194